Fuel 334 (2023) 126734

Contents lists available at ScienceDirect

Fuel

journal homepage: www.elsevier.com/locate/fuel

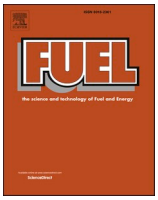

Post-plasma quenching to improve conversion and energy efficiency in a CO_2 microwave plasma

E.R. Mercer [a,b,*], S. Van Alphen [a,e,*], C.F.A.M. van Deursen [b], T.W.H. Righart [d], W.A. Bongers [b], R. Snyders [e,f], A. Bogaerts [a], M.C.M. van de Sanden [b,c], F.J.J. Peeters [b]

[a] Research group PLASMANT, Department of Chemistry, University of Antwerp, Universiteitsplein 1, 2610 Antwerpen, Belgium
[b] Research Group PSFD, Dutch Institute of Fundamental Energy Research, De Zaale 20, 5612 AJ Eindhoven, Netherlands
[c] Eindhoven Institute for Renewable Energy Systems, Eindhoven University of Technology, P.O. Box 513, 5600 MB Eindhoven, The Netherlands
[d] Plasma Chemistry, Department of Circular Chemical Engineering, Faculty of Science and Engineering, Maastricht University, PO Box 616, 6200 MD Maastricht, The Netherlands
[e] Research group ChIPS, Department of Chemistry, University of Mons, 20, Place du parc, 7000 Mons, Belgium
[f] Materia Nova Research Center, 3 Avenue Nicolas Copernic, 7000 Mons, Belgium

ARTICLE INFO

Keywords:
Plasma-based conversion
CO_2 dissociation
CO_2 conversion
Power-2-X
Thermal plasma
Nozzle

ABSTRACT

Transforming CO_2 into value-added chemicals is crucial to realizing a carbon–neutral economy, and plasma-based conversion, a Power-2-X technology, offers a promising route to realizing an efficient and scalable process. This paper investigates the effects of post-plasma placement of a converging–diverging nozzle in a vortex-stabilized 2.45 GHz CO_2 microwave plasma reactor to increase energy efficiency and conversion. The CDN leads to a 21 % relative increase in energy efficiency (31 %) and CO_2 conversion (13 %) at high flow rates and near-atmospheric conditions. The most significant performance improvement was seen at low flow rates and sub-atmospheric pressure (300 mbar), where energy efficiency was 23 % and conversion was 28 %, a 71 % relative increase over conditions without the CDN. Using CFD simulations, we found that the CDN produces a change in the flow geometry, leading to a confined temperature profile at the height of the plasma, and forced extraction of CO to the post-CDN region.

1. Introduction

In 1998, *Hoffert et al.* published a letter to Nature outlining the importance of meeting 10 TW of carbon-free energy sources by 2050 [1]. In 1998, society produced 1.2 TW of carbon-free energy versus 11.7 TW of carbon-emitting power sources. In the most recent report from 2019, only 1.8 TW of carbon-free energy was created versus 17.7 TW of carbon-emitting energy [2]. This data tells us that we have increased our dependence on carbon-emitting power without regard to the warnings issued more than two decades ago. Drastic changes must be made in transitioning our society to be carbon neutral.

Power-to-X (P2X) pathways utilize renewable energy by decoupling the power generated from the electricity sector, moving us toward decarbonization and thus pushing our society closer to a low-carbon economy. One P2X pathway is plasmolysis, which converts green electricity into value-added chemicals for storage by dissociating captured CO_2 into CO as a precursor to synthetic fuels. Many technologies already exist to create synthetic hydrocarbons from CO, such as the water–gas shift reaction, which produces H_2, followed by the well-known Fischer-Tropsch synthesis, which reacts CO with H_2 to produce hydrocarbon chains. Since plasmolysis can match intermittent renewable energies with a high power density through on/off switching, variable green energy sources can be converted into precursors for synthetic liquid fuels. Plasma reactors have the potential to be designed for use in local or regional energy infrastructure, making for a promising approach to chemical conversion.

Efforts to study the dissociation of CO_2 into CO using microwave (MW) plasma reactors, or plasmolysis, have become the focus of much research, as these devices offer energy efficiencies for reducing CO_2 to CO approaching the thermodynamic limit of ~ 50 %. It has been theorized that MW plasma could exceed this limit through super-ideal quenching [3–5]. Although results from MW plasmas are encouraging, the conversion degree (defined as the fraction of CO_2 converted in a single pass through the reactor) depends critically on operating

* Corresponding authors at: Research group PLASMANT, Department of Chemistry, University of Antwerp, Universiteitsplein 1, 2610 Antwerpen, Belgium.
E-mail addresses: elizabeth.mercer@uantwerpen.be (E.R. Mercer), senne.vanalphen@uantwerpen.be (S. Van Alphen).

https://doi.org/10.1016/j.fuel.2022.126734
Received 10 September 2022; Received in revised form 1 November 2022; Accepted 10 November 2022
Available online 26 November 2022

conditions [6–8]. As pressure increases, there is a general drop-off in conversion due to increased collisional recombination mechanisms, posing a fundamental issue for industrialized plasmolysis. To avoid running MW plasma reactors under vacuum, which is energy-intensive and less cost-effective, achieving higher conversion at atmospheric pressure is crucial for realizing industrialization [3]. Recent studies suggest that if the post-plasma gas undergoes a *quenching* step, converted CO can be conserved and, in some cases, increased [9–11]. Quenching is defined here as a sufficiently rapid reduction in (local) gas temperature to prevent reactions of CO with O or O_2 back to CO_2.

A 2017 paper by *van Rooij et al.* outlined a case study on CO_2 splitting using plasmolysis, concluding that given the difficulty of separating CO from the effluent mixture, improving conversion is the most effective way to lower operation costs for CO_2 plasma dissociation [12]. A relatively low flow rate, i.e., high power-to-flow ratio, also called specific energy input (SEI; $SEI = P(W)/\phi_{CO_2}(slm)$), generally correlates with a high conversion rate; however, this simultaneously leads to an increased average gas temperature in the effluent, which makes quenching the mixture to 'freeze-in' the CO produced more difficult. Moreover, a high conversion implies higher CO and O species concentrations, further accelerating back reaction rates. Recent studies show efficiency limits are likely the result of recombination in the post-plasma region and not production limitations in the plasma itself, further emphasizing the need for improved quenching strategies [4].

By studying temperatures in and around the plasma and in the post-plasma region, we can better understand how to optimize quenching [9]. 0D kinetic models have shown that a post-plasma cooling rate is optimal at 10^6 or 10^7 $K.s^{-1}$ with an assumed starting temperature up to 6000 K [9–11,13]. One interesting quenching method is introducing a nozzle in the post-plasma region, designed to induce additional mixing of the inhomogeneously heated gas surrounding the plasma. This method rapidly cools the effluent's hottest areas by using gas in colder regions to reduce the CO backreaction rate [11].

In MW plasmas, the core plasma temperature (T_{core}) can exceed 5000 K, with temperatures in the surrounding region well above 3000 K. It has been confirmed that MW plasmas under these conditions are fully thermalized and strongly inhomogeneous [4,16]. The inhomogeneous behavior is characterized by cylindrical symmetry within the reactor, with the radial direction dominated by turbulent transport and the axial direction dominated by the convective transport of molecules.

The T_{core} and the surrounding area dictate the density of species that enter the post-plasma region or 'effluent stream'. Near the plasma (z = 0 mm) at temperatures above ~ 3000 K, thermal conversion of CO_2 to CO is considered significant (Fig. 1) [14]. We define the area near the plasma where the temperature is above this threshold as the *zone of conversion*, where CO molecules typically outnumber CO_2.

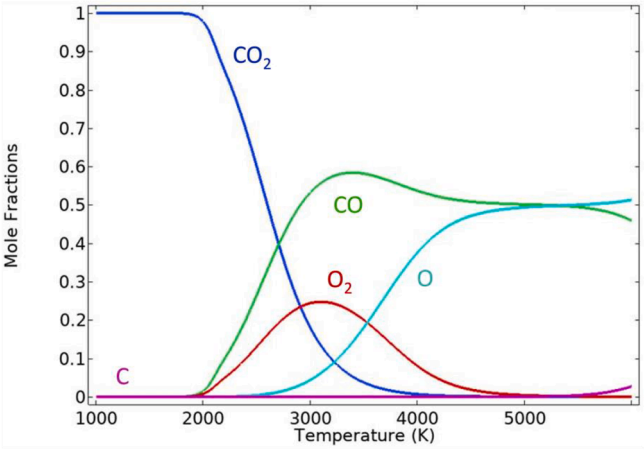

Fig. 1. Figure 1 shows the mole fractions of dominant species at a given temperature (K), calculated using the chemistry set defined in SI, Section S.1, when thermo-equilibrium is reached.

The temperature profile within the reactor peaks with T_{core} and begins a steady decrease radially and axially from the plasma region. Once the temperature drops below ~ 3000 K, CO to CO_2 net recombination competes with dissociation pathways, and energy efficiency may be lost to recombination mechanisms. The reader should remember that dissociation and recombination co-occur under these conditions. Still, as we investigate the effects of these mechanisms, we define temperature profiles at which the pathway to conversion or recombination dominates. We describe the '*zone of recombination*', where the temperature is between 2000 and 3000 K, and the dominant pathway is the recombination of CO with atomic O. If the cooling trajectory in the post-plasma temperature can be quickly quenched to below 2000 K, O association to O_2 occurs faster than recombination to CO_2, and thus more CO would be retained, given that CO recombination with O_2 has a significant reaction barrier.

It is crucial to note that the required time for chemical reactions to achieve the equilibrium composition depicted in Fig. 1 is significantly shorter than the residence time of the gas in the *zone of conversion*, as concluded in the 2D axisymmetric model of our plasma reactor presented in [3]. Especially at increased pressures (p > 200 mbar), residence times in the *zone of conversion* are expected to be > 0.1 ms, while the time required to achieve chemical equilibrium is < 0.01 ms at temperatures of 4000 K and above [13]. This implies that the production of CO within the plasma region is not a limiting factor, and the conversion achieved in the reactor is mainly a function of post-plasma recombination.

This paper aims to provide insight into optimizing the conversion and energy efficiency through an analysis of post-plasma quenching by enhanced mixing using a converging–diverging nozzle (CDN), specifically through the study of the temperature profile of the plasma region, or the *zone of conversion*, as well as the temperature profile in the post-plasma, or effluent, region of the reactor. This analysis is further enhanced with a 3D computational fluid dynamics (CFD) model in COMSOL Multiphysics, which allows for detailed analysis of the flow geometry without and with the CDN to investigate how molecular transport around the plasma is affected by the nozzle.

2. Materials and methods

2.1. Experimental setup

The experiments were carried out in a vortex-stabilized MW reactor with a 2.45 GHz magnetron (Frick und Mallah MKO 2 kW AC002). The configuration exploits a forward vortex to confine and stabilize the plasma. The magnetron emits an adjustable continuous wave (CW) power set to 1300 W transmitted through a WR340 rectangular waveguide in a transverse electric mode (TE_{10}) standing wave, such that the electric field is parallel to the overall gas flow direction. An automatic stub tuner (HOMER S-TEAM STHT2450) between the magnetron source and quartz tube ensures a high coupling efficiency by matching the impedance of the source to the plasma, such that reflected power remains below 1 % during experiments. Further details of the setup can be referenced in Supporting Information, Section S.2.

Fig. 2 shows the configuration of the tangential injection of CO_2 with matching gas inlet diameters of 0.9 mm. The flow geometry inside the quartz tube is strongly affected by the tangential injection of CO_2 at the top of the reactor, creating a vortex around the axis of the tube [3,14,16]. The vortex maintains rotational symmetry of the temperature profile centering the discharge, and by extension, the neutral density profile. [3]. This protects the quartz tube wall from the extreme heat of the plasma. The vortex's complex flow pattern affects molecular and heat transport rates from the plasma [17]. The center of the waveguide is measured to be 65 mm from the gas inlet.

The CDN is an hourglass-shaped nozzle fabricated from grade 304 stainless steel. The CDN is designed to reduce the fluid flow area to a

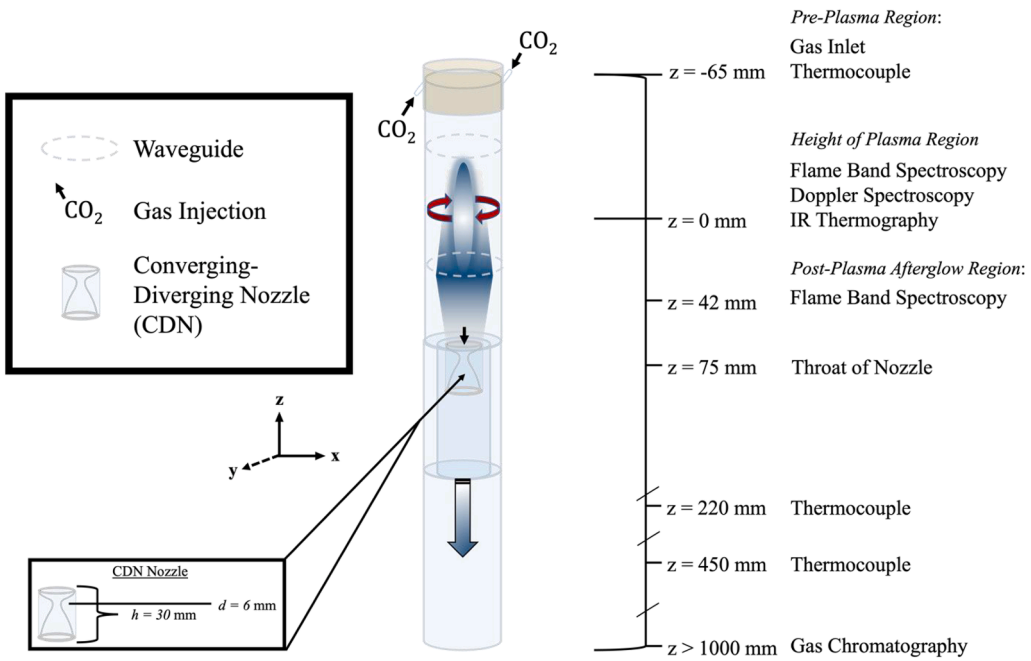

Fig. 2. Setup overview with relative distances of the diagnostics from the plasma, as well as the placement of the CDN from the plasma region.

minimum at the nozzle's innermost diameter or throat. This design causes an increase in the flow velocity as a fluid moves through the converging side to the throat and expands outward on the diverging side of the CDN. The innermost diameter of the nozzle is 6 mm and is situated 10 mm from the top of the nozzle. The CDN has a height of 30 mm, an outer diameter of 25 mm, and is placed 75 mm from the center of the waveguide within a water-cooled metal housing; however, cooling of the CDN is considered negligible as confirmed by the measured power loss within the water cooling system. Details on the nozzle and metal housing can be referenced in Supporting Information, Section S.2.

2.2. Temperature measurements

Using the principle of Doppler broadening of the 777 nm oxygen triplet emission lines, $O(3s^5S^0 \leftarrow 3p^5P)$, at 777.539, 777.417, and 777.194 nm, T_{core} was determined [14,16,18]. Since Doppler broadening is only suitable for measuring electronically excited O atoms, flame band spectroscopy was utilized as a secondary temperature diagnostic to capture the temperature around the plasma and in the afterglow, where virtually no electronically excited O atoms are present [19,20]. Flame band spectroscopy measures the emission intensity from the radiative transition of excited CO_2 to ground-state CO_2 after recombination.

The radially-averaged temperature ($\langle T_{rad} \rangle$) at the height of the plasma and in the afterglow region downstream is calculated using:

$$\langle T_{rad} \rangle = \frac{\int_0^r 2\pi r T(r) n_{neutral}(r) dr}{\int_0^r 2\pi r n_{neutral}(r) dr} = \frac{\int_0^r r dr}{\int_0^r \frac{r}{T(r)} dr} \quad (1)$$

where $T(r)$ is the temperature as a function of the radius, as given by the measurements from Doppler broadening spectroscopy (at the height of the plasma, Fig. 2) and flame band spectroscopy (at the height of the plasma and in the afterglow region, Fig. 2). The neutral gas number density ($n_{neutral}(r)$) is used as a weight factor for the measured temperatures to obtain a neutral-density-weighted temperature assuming isobaric conditions, where $n_{neutral}(r) = p/(k \bullet T(r))$, with k the Boltzmann constant. At the height of the plasma, the Doppler measurements give the T_{core} at r = 0 mm (Fig. 2). To account for the temperature gradient between the center of the quartz tube (r = 0 mm) and the first flame band measurement ($r = \pm 1 - 13$ mm), which could vary depending on the temperature in the region surrounding the plasma, a spline interpolation is used between the data points.

K-type thermocouples are used to measure the gas temperature of the surrounding air at the gas inlet in the primary manifold and below the CDN at 220 mm and 450 mm from the plasma. In principle, the measured temperature of the thermocouples is not equal to the gas temperature due to convective and radiative heat transfer with the gas; however, these effects for temperatures below 1000 K are expected to be low [21]. Due to the expected turbulent mixing of the gas, the recorded temperatures are considered the average temperature of the mixture downstream of the plasma, with an error of ± 50 K.

Additional information about temperature-related diagnostics can be referenced in Supporting Information, Section S.3.

2.3. Analytical techniques and performance indicators

Both gas chromatography (GC) and an FDO2 optical oxygen sensor were used to measure the composition of the post-plasma effluent mixture. From this, the degree of dissociation (conversion, α) can be calculated using the following:

$$\alpha = \frac{[CO]}{[CO] + [CO_2]} \quad (2)$$

where [CO] and [CO_2] represent the concentration fractions as taken from the GC. The energy efficiency, η, can be obtained through:

$$\eta = \alpha \frac{\Delta H_f}{SEI} \quad (3)$$

where ΔH_f is the formation enthalpy of the net reduction reaction of CO_2 to CO (S.R5), and *SEI* is the specific energy input, defined above, and both are given in the same units, e.g., eV.molecule^{-1}. Further details on both the analytical techniques and performance calculations are outlined in Supporting Information, Section S4 and S5, respectively.

2.4. Modeling the gas flow behavior and gas heating

To reveal the effect of the CDN on the flow pattern and the heat transfer inside the plasma and effluent, we developed a reacting flow

model that calculates the gas flow velocity and gas temperature inside the MW reactor within COMSOL Multiphysics 6.0. The gas flow behavior is described using a Reynolds-Averaged Navier Stokes (RANS) Shear Stress Transport (SST) turbulent gas flow model that solves the following mass continuity and momentum continuity equations for a Newtonian fluid:

$$\nabla \bullet (\rho_g \overrightarrow{u_g}) = 0 \tag{4}$$

$$\rho_g(\overrightarrow{u_g} \bullet \nabla)\overrightarrow{u_g} = \nabla \bullet \left[-p\overrightarrow{I} + (\mu + \mu_T)(\nabla \overrightarrow{u_g} + \nabla\left((\overrightarrow{u_g})^T\right) - \frac{2}{3}(\mu + \mu_T)(\nabla \bullet \overrightarrow{u_g})\overrightarrow{I} - \frac{2}{3}\rho_g k_T \overrightarrow{I} \right] + \overrightarrow{F} \tag{5}$$

where ρ_g stands for the gas density, $\overrightarrow{u_g}$ is the gas flow velocity vector, superscript T stands for transposition, p is the gas pressure, μ is the dynamic viscosity, and μ_T the turbulent viscosity of the compressible fluid, k_T is the turbulent kinetic energy, $\overrightarrow{I}$ the unity tensor and $\overrightarrow{F}$ the body force vector. More information on the turbulent gas flow model and the equations for calculating the turbulent kinetic energy are given in the Supporting Information, Section S.6.

The following thermal balance equation calculates the gas temperature:

$$C_p \frac{\partial T}{\partial t} + \rho_m C_p \overrightarrow{u}_g \bullet \nabla T + \nabla \bullet \overrightarrow{q} = Q \tag{6}$$

where ρ_m stands for the mass density, C_p for the isobaric heat capacity, T is the temperature, $\overrightarrow{u}_g$ the gas velocity field vector, and $\overrightarrow{q}$ the heat flux vector, which is calculated by:

$$\overrightarrow{q} = -k\nabla T \tag{7}$$

where k is the thermal conductivity, the material properties μ, C_p, and k in equations E5, E6, and E7, respectively, are adopted from *Magin et al.* [22], where these properties are calculated for a wide range of temperatures assuming thermodynamic equilibrium.

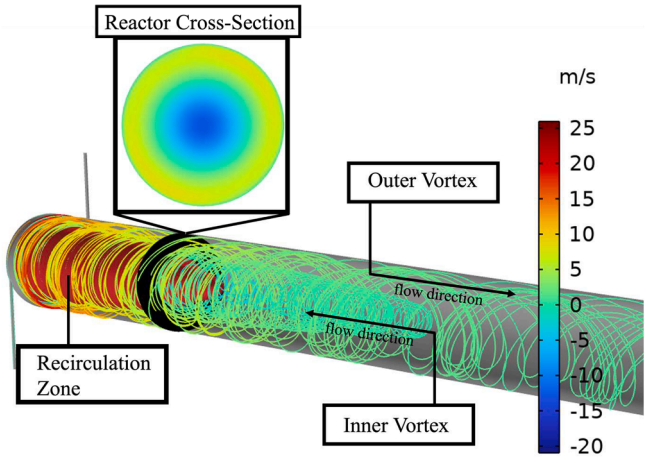

Fig. 3. Calculated gas streamlines within the MW reactor for a flow rate of 15 slm at 700 mbar without CDN attached. The outer and inner vortex is indicated (black arrow), as well as the recirculation zone (red cone). A cross-sectional depiction of the reactor at z = 0 mm is given to show the radial variation of the flow field. (For interpretation of the references to colour in this figure legend, the reader is referred to the web version of this article.)

The thermal balance equation [E6] holds the heat source term (Q), representing the absorbed MW power. This source term is calculated assuming that the power provided by the MW source is nearly fully transferred to gas heating, which is reasonable given the very fast vibrational-translational relaxation leading to a quasi-thermal plasma regime [17]. Q's radial and axial shape are described by Gaussian functions such that they match the radial and axial plasma dimensions measured by *Wolf et al.* and confirmed by *van de Steeg* [14]. These functions are normalized such that integration of Q ($W.m^{-3}$) over the plasma volume (m^3) yields the experimentally measured plasma power (W).

Fig. 3 shows the calculated streamlines in the MW reactor for a flow rate of 15 slm operating at a pressure of 700 mbar without CDN attached. As shown by the figure, gas is introduced tangentially at high gas flow velocities in the reactor, creating a high-velocity outer vortex stream near the walls. This high-velocity stream gradually slows down, eventually flowing inwards toward the center of the reactor, creating a second inner vortex in the opposite direction. This configuration confines and stabilizes the plasma, creating a hot recirculation zone at the start of the reactor.

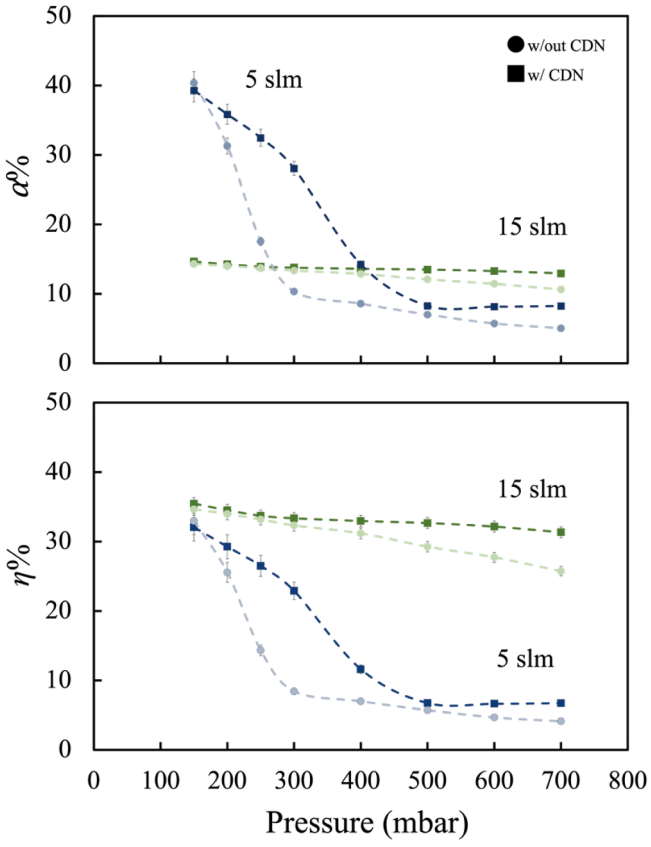

Fig. 4. Conversion (α, top graph) and energy efficiency (η, bottom graph) as a function of pressure (mbar) at two different flow rates (ϕ = 5 and 15 slm) and a constant P = 1300 W, including error bars (although some are too small to be visible, especially at higher pressure).

3. Results and discussion

All results in this section are presented for an input power (P) of 1300 W, at a varying pressure (p) range between 150 and 700 mbar for a 2.45 GHz MW plasma reactor. The work described outlines two flow conditions, 5 and 15 slm, without and with the inclusion of a CDN. The reactor performance (in terms of α and η) is compared with an analysis of the gas temperature profile (both radial and axial) as it relates to the molar fraction of CO, followed by an examination of the flow geometry and its effect on the production of CO.

3.1. Energy efficiency and conversion without and with a CDN

Fig. 4 shows α and η as a function of pressure without and with a CDN compared for two flow rates, $\phi = 5$ and 15 slm, at a constant $P = 1300$ W.

When considering Fig. 4, it is important to observe that both without and with the CDN, there is a decrease in α and η as pressure increases. This pressure-dependent characteristic results from increased back-reactions from molecular three-body collisions [3]. Experimental observations show that as the flow rate is increased (i.e., $\phi = 15$ slm vs $\phi = 5$ slm), the axial cooling trajectory is influenced by a decrease in the molecular residence time and mixing of cooler periphery flows with the hottest center region increases the CO retention in the post-plasma afterglow [3]. A more considerable decay in α is seen predominately at a $\phi = 5$ slm due to 'overheating' in the post-plasma region, where the exothermic back-reaction of CO to CO_2 can create a runaway recombination pathway by maintaining high downstream temperatures, which suppress downstream quenching, furthering the loss of CO. This trend has been outlined in numerous works on MW plasmas and has led to studying how post-plasma quenching can reduce or eliminate this [12,23,24].

We see that with the addition of the CDN, both α and η increase over benchmark conditions in this pressure regime for both flow rates studied. Notably, at $\phi = 5$ slm, the most significant gain in performance is shown to be at 300 mbar, which increases α and η by a factor of 1.7 over benchmark conditions. This gain decreases significantly when the pressure is increased to 400 mbar. In the following discussion, we will investigate the performance at $\phi = 5$ slm as a function of pressure by examining the temperature profiles, as well as the results at $\phi = 15$ slm, focusing on the effects when $p = 700$ mbar and an increase by a factor of 1.2 is observed for α and η (Fig. 4).

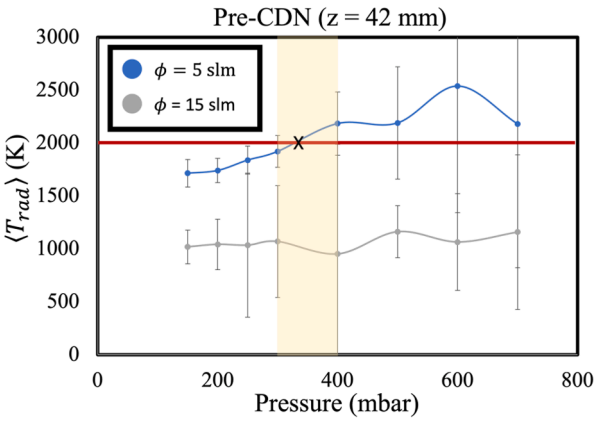

Fig. 6. $\langle T_{rad} \rangle$ as a function of pressure for two different flow rates pre-CDN (z = 42 mm) (left). The red line indicates the temperature at which recombination to CO_2 is quenched most effectively (Fig. 1). The highest $\langle T_{rad} \rangle$ is found for $\phi = 5$ slm, and between p = 300 mbar and p = 400 mbar $\langle T_{rad} \rangle$ rises above 2000 K, which is correlated with a decrease in α. (For interpretation of the references to colour in this figure legend, the reader is referred to the web version of this article.)

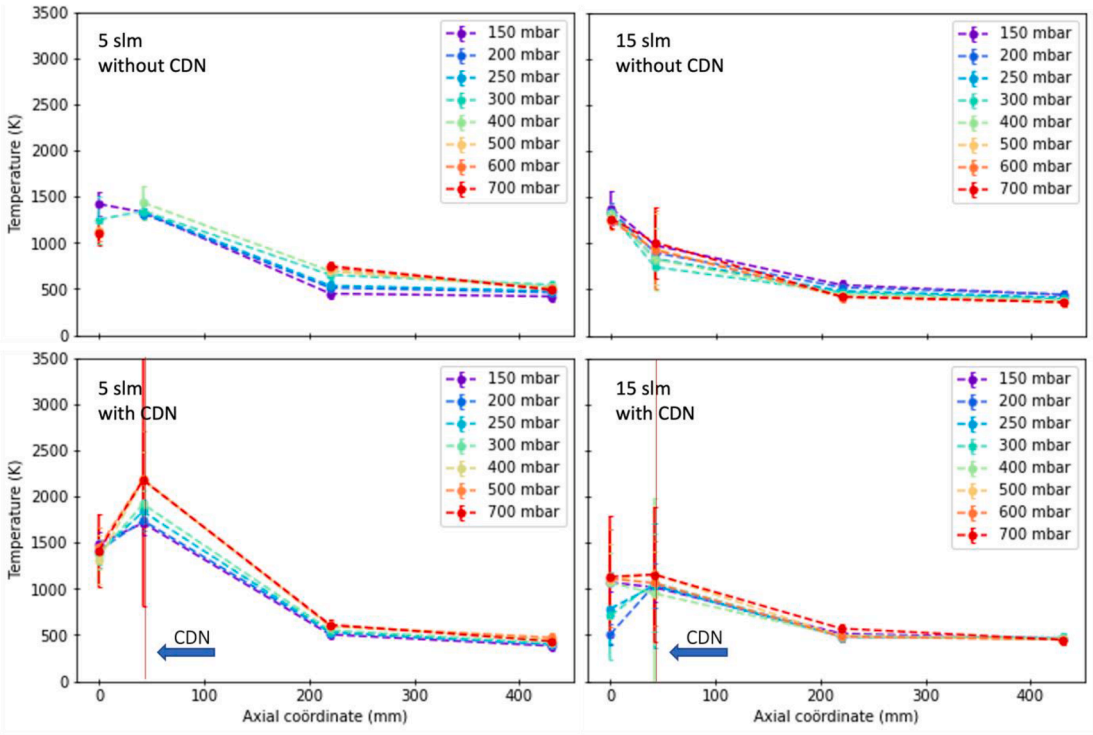

Fig. 5. Evolution of (radially-averaged) temperature, $\langle T_{rad} \rangle$, at several axial positions for $\phi = 5$ slm (left graphs) and 15 slm (right graphs) without (top graphs) and with the CDN (bottom graphs) at different pressures, as indicated by the legend. The error bars are also indicated but sometimes are too small to be visible (at z = 220 and 450 mm). The red line indicates the approximate CDN placement (bottom graphs). (For interpretation of the references to colour in this figure legend, the reader is referred to the web version of this article.)

3.2. Effect of the Converging-Diverging nozzle on Post-Plasma quenching

3.2.1. Analysis of the temperature profile

In Fig. 5, the radially-averaged temperature profile, $\langle T_{rad} \rangle$, obtained from [E1], at respective axial positions from the plasma is plotted, in comparison without and with the CDN for $\phi = 5$ and 15 slm at varying pressures, to show the cooling trajectory.

In Fig. 5, we find that with the CDN at $\phi = 5$ slm there is an increase in the pre-CDN $\langle T_{rad} \rangle$ (at $z = 0$ and 42 mm) compared to without the CDN. However, there is faster post-plasma cooling, and the increase in $\langle T_{rad} \rangle$ when $p > 300$ mbar coincides with a decrease in α (Fig. 4). We also observe that this decay begins after $\langle T_{rad} \rangle > 2000$ K. To investigate the effects that the CDN has on the pre-CDN and post-CDN temperature, $\langle T_{rad} \rangle$ at $z = 42$ mm (~33 mm above the throat of the CDN) and $z = 220$ mm (~145 mm below the throat of the nozzle) is plotted as a function of pressure in Fig. 6.

A $\langle T_{rad} \rangle > 2000$ K pre-CDN is generally only found at $\phi = 5$ slm and $p > 300$ mbar, where α significantly drops (cf. Fig. 4 above). This indicates that overheating in the pre-CDN region is detrimental to α (Fig. 4). Thus, controlling the plasma temperature within the reactor is essential for improving α. When considering $\phi = 15$ slm, we find that the CDN does not increase the cooling rate (cf. Fig. 5). The most significant change in α and η is observed at $\phi = 5$ slm and $p = 300$ mbar, where the performance increases by a factor of 1.7 with the CDN compared to without the CDN and decreases significantly when the pressure is increased to $p = 400$ mbar (Fig. 4 *above*). Understanding that recombination to CO_2 occurs rapidly within the cooling trajectory in the post-plasma region, we further analyzed the radial temperature profile, *T(r)*, at $z = 42$ mm, as measured by flame band spectroscopy for $\phi = 5$ slm at $p = 300$ and 400 mbar, where we observed higher $\langle T_{rad} \rangle$ and a large decrease in α between these pressures.

The values of *T(r)* without and with the CDN at $p = 300$ and 400 mbar are shown in Fig. 7, where an increase in temperature with the CDN is observed over conditions without the CDN. Without the CDN, it is observed that *T(r)* does not show a significant change with pressure; however, with the CDN, *T(r)* at $p = 400$ mbar is much broader than at $p = 300$ mbar. *T(r)* at $p = 400$ mbar shows peaks above 2500 K. Thus, quenching with periphery flows is suppressed, and these conditions are likely indicative of runaway recombination, which is an exothermic process resulting in a significant loss of CO, and helps confirm that overheating in the *zone of conversion* is detrimental to achieving higher α and η. This takes place before the gas can move through the nozzle and increases with increasing pressure, likely due to (CO + O + M) collisional recombination into CO_2. We also observe this with the axial cooling trajectory reported in Fig. 5.

3.3. Effect of the Converging-Diverging nozzle on the height of plasma region

3.3.1. Analysis using the measured temperature profile

When the CDN is introduced into the post-plasma region, η and α increase (Fig. 4). When considering the temperature at the height of the plasma ($z = 0$ mm, Fig. 2) as a function of the radius with and without the CDN, confinement of the temperature profile is observed with the addition of the CDN (Fig. 8).

Fig. 8 shows the *T(r)* without (top graphs) and with the CDN (bottom graphs), where T_{core} at $r = 0$ mm is provided from the Doppler broadening measurement, and the other measurements of *T(r)* are given using flame band measurements with $r_{max} = \pm 13$ mm. Without the CDN, *T(r)* is broader and takes on a Gaussian-like shape, with T_{core} increasing with pressure. There is also a flat temperature profile as the gas approaches the wall, which is especially prevalent at $\phi = 15$ slm.

The bottom graphs in Fig. 8 demonstrate that the addition of the CDN alters the shape of the *T(r)* profile, confining the innermost *T(r)* while increasing the temperature near the walls. We find that although there is confinement in the *T(r)* profile in the *zone of conversion* with the addition of the CDN (Fig. 8), an increase in α is observed (Fig. 4); therefore, the CDN must compensate for the smaller *zone of conversion*. In other words, a narrower temperature profile in the radial direction is correlated to a higher reported α, if $\langle T_{rad} \rangle$ also remains below 2000 K.

3.3.2. Analysis using the 3D computational fluid dynamics model

Using our 3D CFD simulations, we calculated the cross-sectional temperature profile over the entire reactor for $\phi = 15$ slm at 700 mbar, shown in Fig. 9.

The black line in Fig. 9 indicates where $T = 3000$ K, and we consider the zone within this line as the *zone of conversion* for the two configurations. Visually, the temperature around the plasma region becomes more confined with the CDN, and a sharper gradient is observed between the *zone of conversion* and the area near the walls of the quartz tube. There is generally a good agreement between the temperature profiles found experimentally and within the model, as we also observe this in the experimental results reported in Fig. 8.

When comparing the cases with and without the CDN, the temperature confinement around the height of the plasma becomes more defined with CDN. As discussed previously, the higher α found with the CDN is not due to an increase in the radial temperature profile (or, in other words, an increase in the volume of the *zone of conversion*) at the

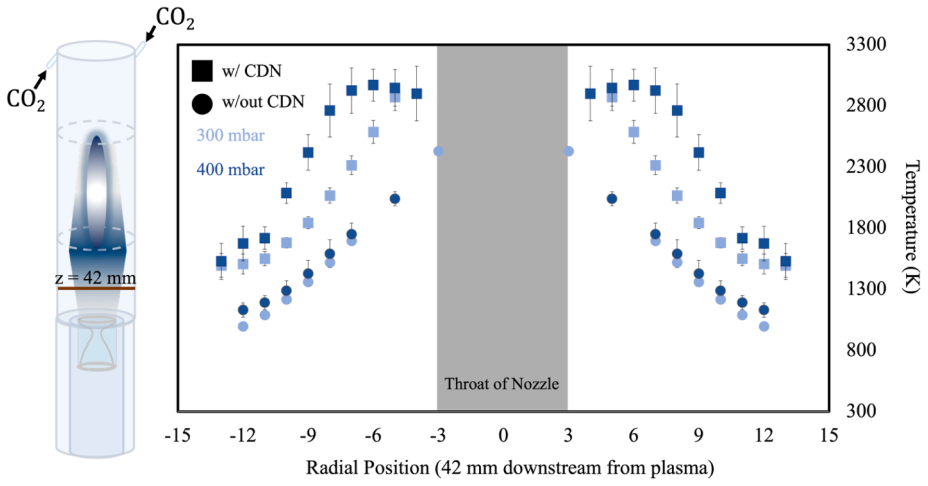

Fig. 7. Radial temperature profile, T(r), 42 mm downstream from plasma, as measured by flame band spectroscopy, without and with CDN, for ϕ = 5 slm at two pressures, p = 300 (light blue) and p = 400 mbar (dark blue) with accompanied schematic for the placement of the measurement. (For interpretation of the references to colour in this figure legend, the reader is referred to the web version of this article.)

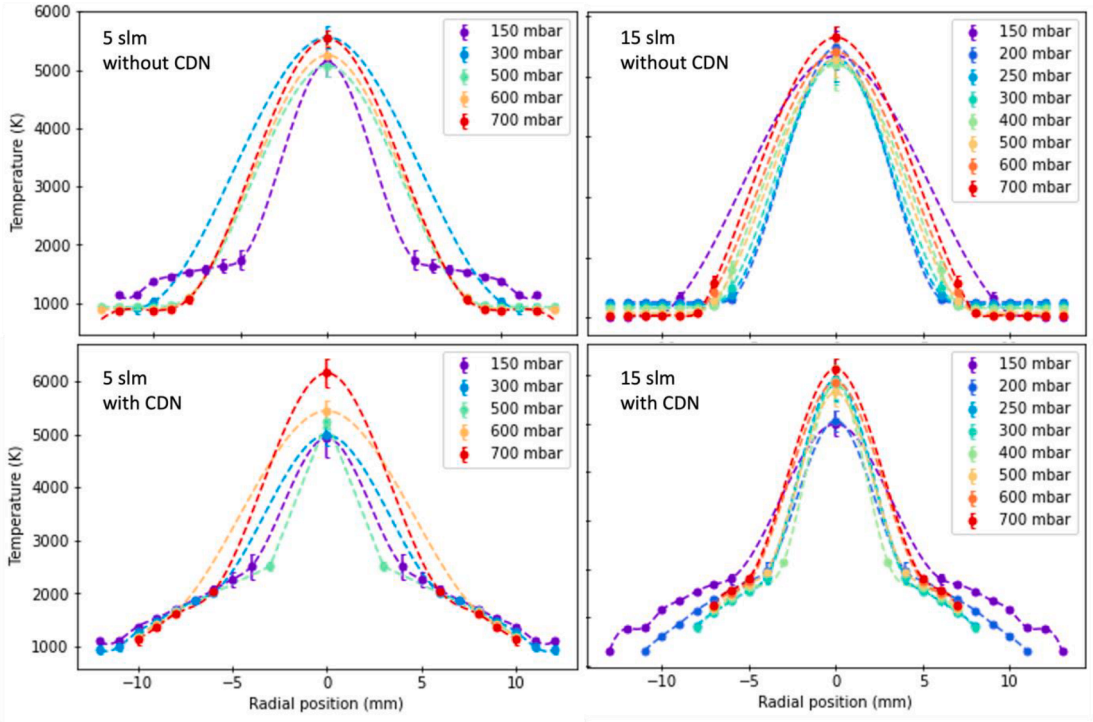

Fig. 8. Measured T(r) profile at the height of the plasma (z = 0 mm) for ϕ = 5 slm (left) and 15 slm (right) at varying pressure, where the peak represents the T_{core} (Doppler broadening measurement) and the outer data points approach the edge of the quartz tube (flame band measurement, r_{max} = 13 mm). Note that the profiles without the CDN (top graphs) are broader than the profiles with the CDN (bottom graphs).

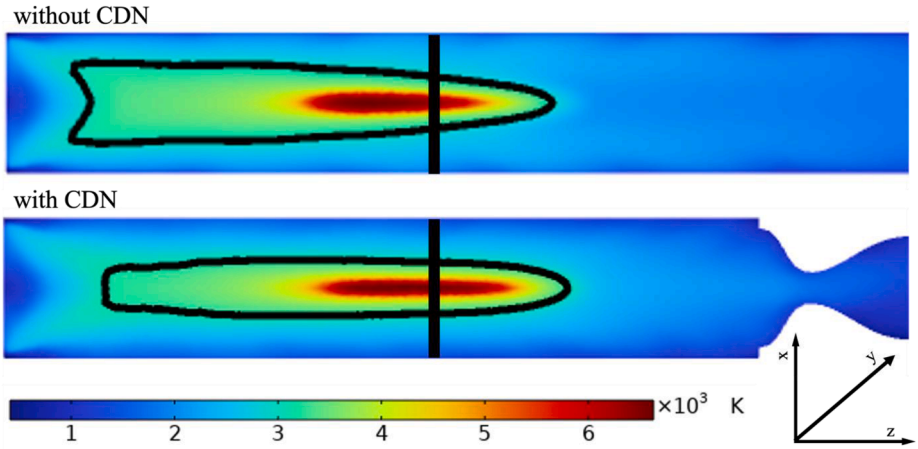

Fig. 9. Calculated cross-sectional temperature profile, without and with CDN, for ϕ = 15 slm at 700 mbar. The black line indicates where the temperature is 3000 K, with a line running through the x-direction indicating z = 0 mm.

height of the plasma. Therefore, the total influence of the CDN on the flow geometry should be considered. An overlay of the calculated velocity streamlines (black lines) and the recirculation zone where the flow velocity moves upstream (white line, negative-z-direction) is illustrated in Fig. 10.

Fig. 10 shows a velocity field moving upward through the center of the plasma region in both cases, bounded by the white line (see figure caption). From the center, the gas first flows towards the plane of injection before moving downstream (positive z-direction, outside the white line) near the walls. We observe recirculation cells, which are indicated by the black swirls standing between the border where the flow direction changes (shown by the white lines) in Fig. 10. We find that these border recirculation cells are increased with the CDN, indicating an enhanced mixing between cold injected gas (moving downstream near the tube wall) and the zone of conversion (located within the central inner vortex).

The CDN also appears to disrupt the flow geometry by 'pinching' the inner vortex (cf. Fig. 3) upwards towards the plane of injection, which can be attributed to the convergence of the downstream flow to the throat of the CDN. This disruption to flow extends upwards towards the top of the reactor through a center streamline, contracting the inner vortex traditionally found in a forward vortex configuration (Fig. 3). In other words, the outer vortex is forced towards the center of the reactor as it approaches the CDN, confining the temperature profile we observed as the black line in Fig. 9 to a smaller but hotter area. For the reactor with the CDN, the highlighted inner vortex is much smaller and concentrated in the plasma's hotter region and the higher temperature zone. Without the CDN, CO created in the *zone of conversion* has the

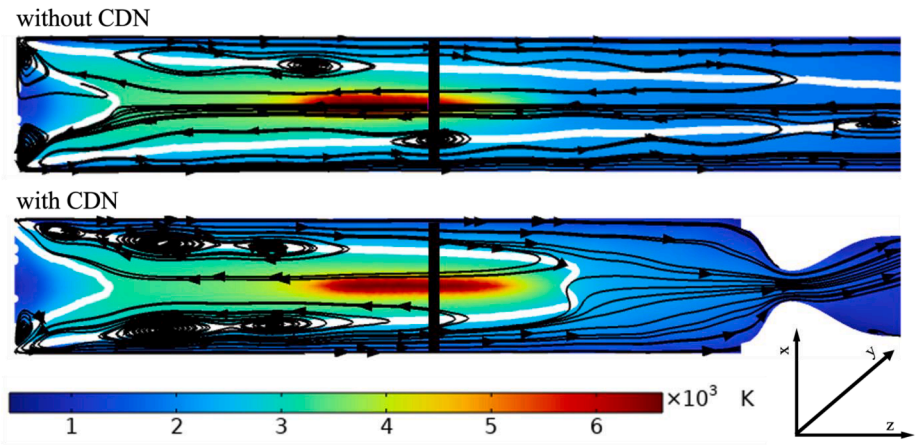

Fig. 10. Calculated 2D temperature profile in a reactor cross-section without and with a CDN for ϕ = 15 slm at 700 mbar. The black arrows represent the direction of the gas flow velocities and velocity field streamlines; the white line represents the field within which the z-velocity < 0, meaning that gas flows upwards (negative-z-direction, cf. Fig. 3) and falls along recirculation cells (i.e., the black cyclones straddling the interface between the two directions of flow). The black line in the x-direction indicates z = 0 mm.

opportunity to flow upwards again via the long inner vortex, returning to the *zone of conversion*. By contrast, with the introduction of the CDN, the inner vortex is significantly shortened and therefore matches the length of the *zone of conversion*. This suggests that once CO is formed in the *zone of conversion* and is circulated towards the wall of the quartz tube (cf. Fig. 3), the CO will be directed towards the reactor exit. Moreover, the more confined temperature profile in the radial direction implies a stronger concentration gradient of CO in this direction, and hence a greater radial diffusive driving force for CO transport than would be found in the absence of a CDN, where the gradient is weaker. Confirming this enhanced driving force for radial diffusion will require including chemical kinetics and individual species transport in the model; however, this is beyond the scope of the current manuscript.

In Fig. 9, we observe that the radial temperature profile just below the *zone of conversion* with and without CDN are quite similar; therefore, the CDN does not directly enhance the post-plasma mixing of hotter gas with colder gas, as even without CDN, this post-plasma mixing already occurs quite effectively. Instead, the CDN ensures that this mixed, uniformly heated gas is directed entirely toward the reactor exit and cannot return upstream via the inner vortex. Insofar as a CDN enhances the mixing of non-uniformly heated gas, this mixing does not occur directly above or within the throat of the CDN but further upstream along the sides of the plasma. Without the CDN, this mixing occurs along a much longer inner vortex and includes cooling of CO, which is recirculated back into the plasma region (c.f. Fig. 9).

4. Conclusion and outlook

In this work, we investigated the effect of adding a converging–diverging nozzle (CDN) to a MW plasma reactor used for CO_2 splitting on the conversion (α) and energy efficiency (η), for a wide pressure range and two different flow rates ($\phi = 5$ and 15 slm).

The experimental data displays a marked increase in α and η with the addition of the CDN. We observe that the axial cooling trajectory of the radially-averaged temperatures, $\langle T_{rad} \rangle$, changes for $\phi = 5$ slm, and this effect was seen less at $\phi = 15$ slm. A correlation between $\langle T_{rad} \rangle > 2000$ K, and a drop in α was also observed. The most significant gain in α at $\phi = 5$ slm and 300 mbar was related to an increase in the temperature gradient (observed in *T(r)*, Fig. 7). This, balanced with the lower pressure reducing collisional recombination to CO_2, is likely the cause of the factor 1.7 increase in α.

Through the CFD simulation, we observe that the CDN induces a change in the flow geometry, where the circulation of the vortex is pinched upwards in the near plasma region, bringing the length of the inner vortex flow more in line with the length of the plasma region. Any CO molecules formed within the plasma region will be transported directly to the exit of the reactor, while in a geometry without a CDN, molecules downstream of the plasma can potentially recirculate back to the plasma region via the inner vortex, which is unlikely to benefit reactor performance, as CO would be repeatedly cooled and reheated without adding to the overall conversion. The more well-defined flow geometry from the CDN results in increased performance, despite the smaller *zone of conversion*, which we suggest could be related to an enhanced radial driving force for CO transport from the *zone of conversion* to the colder gas moving downstream near the quartz tube wall. An increase in the number of local recirculation cells between the tube wall and *zone of conversion* are also observed, which would similarly contribute to this enhanced radial transport. We also observed an increase in $\langle T_{rad} \rangle$ to above 2000 K before the CDN (Fig. 6), indicative of runaway recombination, which is detrimental to α. Therefore, 'overheating' of the pre-CDN temperature should be avoided to minimize recombination to CO_2 and maximize the benefit of the CDN.

Altogether, our experimental and computational results indicate that confining the temperatures at the height of the plasma and reducing the size of the inner vortex to better match the size of the high-temperature *zone of conversion* increases CO yields. These changes can be achieved by adding a constriction, such as a CDN, in the post-plasma region. Placement of the CDN is crucial, as we observed with the axial cooling trajectory. Given that the current placement of the CDN throat is still ~ 3 cm from the bottom of the plasma, future experiments with the placement of the CDN closer to the plasma might show additional improvement by increased heat transfer.

Furthermore, modifications to the CDN, such as configuring the throat of the nozzle to a specific flow rate and pressure (e.g., to reach supersonic expansion quenching conditions), have the potential to enhance the benefits outlined within this work. Further work on the CFD model to realize a fully-coupled chemical kinetic simulation has the potential to give great insight into the mechanisms that play the most significant role in enhancing CO_2 conversion in a CDN-modified flow geometry, especially to uncover the differences in radial transport at the height of the plasma. This would ultimately allow a deeper understanding of how we can further optimize MW plasma-based conversion of CO_2.

CRediT authorship contribution statement

E.R. Mercer: Investigation, Data curation, Writing – original draft, Visualization. **S. Van Alphen:** Methodology, Formal analysis, Writing – original draft. **C.F.A.M. van Deursen:** Investigation, Formal analysis, Data curation. **T.W.H. Righart:** Software. **W.A. Bongers:** Supervision, Resources. **R. Snyders:** Funding acquisition, Writing – review & editing. **A. Bogaerts:** Funding acquisition, Writing – review & editing. **M.C.M. van de Sanden:** Funding acquisition, Writing – review & editing. **F.J.J. Peeters:** Methodology, Supervision, Writing – review & editing.

Declaration of Competing Interest

The authors declare that they have no known competing financial interests or personal relationships that could have appeared to influence the work reported in this paper.

Data availability

Data will be made available on request.

Acknowledgments

This research was supported by the European Research Council (ERC) under the European Union's Horizon 2020 research and innovation program (grant agreement No 810182 – SCOPE ERC Synergy project) and the Excellence of Science FWO-FNRS project (FWO grant ID GoF9618n, EOS ID 30505023). The computational resources and services used in this work were provided by the HPC core facility CalcUA of the Universiteit Antwerpen, and VSC (Flemish Supercomputer Center), funded by the Research Foundation - Flanders (FWO) and the Flemish Government. In addition, this work has been carried out as part of the Plasma Power to Gas research program with reference 15325, which is by the Netherlands Organization for Scientific Research (NWO) and Alliander N.V.

Appendix A. Supplementary data

Supplementary data to this article can be found online at https://doi.org/10.1016/j.fuel.2022.126734.

References

[1] Hoffert MI, Caldeira K, Jain AK, Haites EF, Harvey LDD, Potter SD, et al. Energy implications of future stabilization of atmospheric CO2 content. Nature 1998;395(6705):881–4.
[2] IEA, "CO2 emissions by energy source, World 1990-2019," *IEA*, 2019. https://www.iea.org/data-and-statistics/data-browser/?country=WORLD&fuel=CO2emissions&indicator=CO2BySource (accessed Dec. 01, 2021).
[3] Wolf AJ, Peeters FJJ, Groen PWC, Bongers WA, Van De Sanden MCM. CO2Conversion in nonuniform discharges: disentangling dissociation and recombination mechanisms. J Phys Chem C 2020;124(31):16806–19. https://doi.org/10.1021/ACS.JPCC.0C03637/SUPPL_FILE/JP0C03637_SI_001.PDF.
[4] A. Van De Steeg, P. Viegas, A. Silva, T. Butterworth, A. Van Bavel, and J. Smits, "Redefining the Microwave Plasma Mediated CO 2 Reduction Efficiency Limit : The role of O-CO2 Association," pp. 1–15.
[5] Legasov VA, et al. A nonequilibrium plasma-chemical process of CO2 dissociation in high-frequency and ultrahigh-frequency discharges. Sov Phys Dokl 1978;23:44.
[6] Snoeckx R, Bogaerts A. Plasma technology – a novel solution for CO2 conversion? Chem Soc Rev 2017;46(19):5805–63. https://doi.org/10.1039/C6CS00066E.
[7] Bongers W, et al. Plasma-driven dissociation of CO2 for fuel synthesis. Plasma Process Polym 2016. https://doi.org/10.1002/ppap.201600126.
[8] P. Viegas *et al.*, "Insight into contraction dynamics of microwave plasmas for CO2 conversion," 2020.
[9] Yang T, Shen J, Ran T, Li J, Chen P, Yin Y. Understanding CO2 decomposition by thermal plasma with supersonic expansion quench. Plasma Sci Technol 2018;20(6):65502. https://doi.org/10.1088/2058-6272/aaa969.
[10] Li J, Zhang X, Shen J, Ran T, Chen P, Yin Y. Dissociation of CO2 by thermal plasma with contracting nozzle quenching. J CO2 Util 2017;21:72–6. https://doi.org/10.1016/j.jcou.2017.04.003.
[11] Vermeiren V, Bogaerts A. Plasma-based CO2 conversion: to quench or not to quench? J Phys Chem C 2020;124(34):18401–15. https://doi.org/10.1021/acs.jpcc.0c04257.
[12] van Rooij GJ, Akse HN, Bongers WA, van de Sanden MCM. Plasma for electrification of chemical industry: a case study on CO2 reduction. Plasma Phys Control Fusion 2017;60(1):14019. https://doi.org/10.1088/1361-6587/aa8f7d.
[13] den Harder N, et al. Homogeneous CO2 conversion by microwave plasma: Wave propagation and diagnostics. Plasma Process Polym 2016;14(6):1600120. https://doi.org/10.1002/ppap.201600120.
[14] Wolf AJ, Righart TWH, Peeters FJJ, Bongers WA, Van De Sanden MCM. Implications of thermo-chemical instability on the contracted modes in CO2 microwave plasmas. Plasma Sources Sci Technol 2020;29(2):25005. https://doi.org/10.1088/1361-6595/ab5eca.
[16] Wolf AJ, Righart TWH, Peeters FJJ, Groen PWC, Van De Sanden MCM, Bongers WA. Characterization of CO2 microwave plasma based on the phenomenon of skin-depth-limited contraction. Plasma Sources Sci Technol 2019;28(11):pp. https://doi.org/10.1088/1361-6595/ab4e61.
[17] Wolf AJ, Righart TWH, Peeters FJJ, Bongers WA, van de Sanden MCM. Implications of thermo-chemical instability on the contracted modes in CO2 microwave plasmas. Plasma Sources Sci Technol 2020;29(2):25005. https://doi.org/10.1088/1361-6595/ab5eca.
[18] T. W. H. Righart, "Gas Temperatures adn Residence Times in a Vortex Stabilized CO2 Microwave Plasma," TU/e, 2018.
[19] Raposo G, van de Steeg AW, Mercer ER, van Deursen CFAM, Hendrickx HJL, Bongers WA, et al. Flame Bands: CO + O chemiluminescence as a measure of gas temperature. J Phys D Appl Phys 2021;54(37):374005.
[20] Slack M, Grillo A. High temperature rate coefficient measurements of CO + O chemiluminescence. Combust Flame 1985;59(2):189–96. https://doi.org/10.1016/0010-2180(85)90024-0.
[21] Liu B, Huang Q, Wang P. Influence of surrounding gas temperature on thermocouple measurement. Case Stud Therm Eng 2020;19:100627. https://doi.org/10.1016/j.csite.2020.100627.
[22] T. Magin, G. Degrez, and I. Sokolova, "Thermodynamic and transport properties of martian atmosphere for space entry application," *33rd Plasmadynamics Lasers Conf.*, no. May, 2002, doi: 10.2514/6.2002-2226.
[23] A. J. Wolf, "Thermal aspects of CO2 conversion in the vortex-stabilized microwave plasma.," Technische Universiteit Eindhoven, 2020.
[24] Kelly S, Bogaerts A. Nitrogen fixation in an electrode-free microwave plasma. Joule 2021;5(11):3006–30. https://doi.org/10.1016/j.joule.2021.09.009.